Numerical simulation of the fracture process in concrete resulting from deflagration phenomena

Daisuke FUKUDA[1], Kazuma MORIYA[2], Katsuhiko KANEKO[1], Katsuya SASAKI[3], Ryo SAKAMOTO[3], Keitaro HIDANI[3]

[1] *Faculty of Engineering, Hokkaido University, Kita 13 Nishi 8, Kita-ku, Sapporo, Hokkaido 060-8628, Japan*

[2] *Graduate School of Engineering, Hokkaido University, Kita 13 Nishi 8, Kita-ku, Sapporo, Hokkaido 060-8628, Japan*

[3] *Hitachi Zosen Corporation, 1-7-89 Nanko-kita, Suminoe-ku, Osaka 559-8559, Japan*

*Corresponding author: Daisuke FUKUDA

E-mail: d-fukuda@frontier.hokudai.ac.jp

TEL & FAX: +81-11-706-6302

Abstract

This paper investigated the mechanism of fracture in concrete due to the deflagration phenomenon. For this purpose, the electric discharge impulse crushing method was selected, with liquid nitromethane (NM) taken as the deflagration agent. Employing this technique, NM is set inside charge holes and initiated by electric discharge. The pressure generated by the deflagration of NM in a steel chamber was modeled using the Jones–Wilkins–Lee equation of state. The modeled and measured pressures agreed well and the applicability of the pressure model was validated. Then, assuming controlled splitting along the expected fracture surface in concrete, dynamic fracture process analysis (DFPA) based on two-dimensional dynamic finite element method was conducted. The results showed that fracture patterns predicted in the DFPAs agreed well with those obtained from experiments. The mechanism of fracture in concrete due to deflagration was then discussed in terms of the fracture process in the controlled splitting. Owing to stress interference from each charge hole, compressive stress zones (CSZs) formed above and below the middle regions between charge holes where maximum and minimum principle stresses were both in compression. The CSZs was found to be important in obtaining a flatter fracture surface in the case of controlled splitting. In conclusion, the proposed method was shown to be useful for the investigation of the fracture mechanism in the case of the use of deflagration agents and could be useful for the design optimization of such controlled splitting.

Key words: Dynamic Fracture Process Analysis, Deflagration, Nitromethane, Finite Element Method, Concrete, Material Heterogeneity

1. Introduction

Understanding the mechanism of dynamic fracture in rocks and rock-like materials such as concrete in response to rapidly applied loads is of considerable importance in a wide range of engineering disciplines. Especially in civil and mining engineering, control of fragmentation caused by rapidly applied loads in the case of detonation has been a significant issue because of frequent applications of blasting in, for example, tunnel and mining excavations. Many research papers and books on this topic have been published (e.g., Bhandari 1970; Borovikov and Vanyagin 1995; Bulson 1997; Stiehr and Dean 2011).

However, because of the occasional limitation of the application of blasting, alternative high-speed fracturing techniques have been proposed and developed. One such technique is the use of pulsed high-voltage electric discharge, which has been extensively studied and implemented for various purposes, such as the disintegration and fragmentation of rock-like materials (e.g., Andres 1989; Weise and Loffler 1993; Bluhm et al. 2000; Hofmann and Weisse 1997; Lisitsyn et al. 1999; Rim et al. 1999; Cho et al. 2006; Narahara et al. 2007; Shao et al. 2010). In addition, the application of deflagration agents has been proposed and the legal regulations relating to such application are more relaxed than those relating to blasting. Examples of deflagration agents are powder mixtures of metal oxide with aluminum causing thermite reaction, and nitromethane (NM). However, there has been no report of investigations of the fracture mechanism based on the detailed modeling of the deflagration process, which could be of engineering interest.

Generally, the process of dynamic fracture in rock-like materials is characterized by the initiation, propagation and intersection of multiple cracks. The resultant fracture pattern in the case of dynamic loading is quite different from that in the case of quasi-static loading. In the case of quasi-static loading, a few predominant cracks and large fragments form, while in the case of dynamic loading, the number of initiated cracks increases with increasing loading rate and many smaller fragments form. Previous studies (e.g., Rossi et al. 1991; Hanchak

et al. 1992) have shown that the main parameters affecting dynamic fracture include the applied loading rate and material heterogeneity. The loading rate has been shown to be a significant factor, especially in the high-strain-rate regime, in characterizing fracturing in concrete (e.g., Abrams 1917; Malvern et al. 1985; Ross et al. 1995; Brara et al. 2001; Grote et al. 2001) and rocks (e.g., Bacon 1962; Rinehardt 1965; Birkimer 1970; Zhang et al. 2000; Cho et al. 2004). Large strength increases were observed with the increasing applied loading rate. In addition, Cho et al. (2003b) reported that such strength increase was affected by the material heterogeneity of rock-like materials in the higher strain-rate regime.

Thus, in the investigation of fracturing in rock-like materials due to deflagration, it is necessary to characterize the corresponding loading rate and consider material heterogeneity.

Recently, numerical methods have been increasingly applied in analyzing fracturing, including extensive use of finite-element-method (FEM)-based simulations. These methods include the FEM featuring the element deletion method (e.g., Hallquist 1998), the FEM featuring the interelement crack method (e.g., Xu et al. 1994; Camacho and Ortiz 1996; Carol et al. 1997; Ortiz and Pandolfi 1999; Ruiz et al. 2000; Gálvez et al. 2002; Segura and Carol 2010) and the extended FEM (e.g., Belytschko and Black 1999; Moës et al. 1999; Belytschko et al. 2001; Stolarska et al. 2001; Song and Belytschko 2009). It has been reported that the latter two methods perform reasonably well (Song et al. 2008) with a careful choice of mesh size and fracture energy. On this basis, we carried out dynamic fracture process analysis (DFPA) based on the two-dimensional (2-D) FEM featuring the interelement crack method (Kaneko et al. 1995; Yamamoto et al. 1999; Cho 2003a; Cho et al. 2003b; Cho et al. 2003c; Cho and Kaneko 2004; Cho et al. 2006; Cho et al. 2008). DFPA simulates multiple crack initiations, crack growth including crack bifurcation, and crack coalescence. The code considers material heterogeneity and the size effect of the strength of the material, both of which play an important role in the simulation of the fracturing process in rock-like materials.

With the above background, this paper investigates detailed loading characteristics and the fracture mechanism relating to deflagration. As a research target, we selected a high-speed splitting method for rock-like materials, termed the electric discharge impulse crushing method (EDICM), which uses both

electric discharge and the deflagration of NM (Sasaki et al. 2011).

The paper is arranged as follows. In the next section, we describe the characteristics of a generated pressure profile obtained from pressure measurement and a method for modeling the pressure resulting from the deflagration of NM. Section 3 introduces the DFPA and, in section 4, we simulate the fracturing in concrete through DFPA with the proposed pressure model, and show that the resultant fracture patterns simulated in DFPA agree well with those obtained in experiments. We also discuss the mechanism of fracturing of a concrete block due to the deflagration of NM. Finally, we close the work by presenting conclusions in Section 5.

2. Modeling of pressure arising from deflagration

2.1. Overview of the EDICM

Pertinent information on the EDICM is presented in the following. For further details, see Sasaki et al. (2011). In the EDICM, the initiation cartridge shown in Fig. 1 is prepared. The cartridge consists of a cylindrical plastic bottle, a cylindrical plastic cap and liquid NM. The cartridge also has a thin metal wire. Initiation is controlled by an electric discharge generator, and electric discharge of 2500 A and 1500 V is applied to the wire through cables. The wire is then vaporized by the electric discharge. As a result, plasma is generated and the deflagration of NM commences. Thus, by setting the initiation cartridges in charge holes (CHs) drilled in a target rock-like material, gas expansion due to deflagration causes fracturing in the target. Although the EDICM uses both electric discharge and deflagration, it has been revealed that the electric discharge itself only acts as an initiator for the deflagration of NM and makes little contribution to the resultant fracture (Sasaki et al. 2011). Thus, this paper only focuses on the deflagration.

2.2. Modeling methodology

We consider it essential to understand the characteristics of the generated pressure. The characteristics of pressure generated in a CH were identified by a simple pressure measurement using a hollow austenite stainless-steel chamber (ISO TR 15510 L No. 6). Figure 2 shows a schematic diagram and photograph of

the chamber. The initiation cartridge for the volume of NM, V_{NM} = 12 mL, was set inside the chamber. The hollow interior (i.e., the CH) was confined by upper and lower flanges. The outer diameter, inner diameter and length in the axial direction of the chamber were 120, 20 and 70 mm, respectively. The generated pressure was measured by piezofilm (PVF_2 11-125-EK made by Dynasen, Inc.) set immediately below the initiation cartridge. Poly (methyl methacrylate) (PMMA) was set below the piezofilm to minimize the undesirable interference of reflected stress waves in the obtained data.

Figure 3 shows the measured pressure profile. The horizontal and vertical axes indicate the time after the electric discharge was applied and the measured pressure, respectively. The pressure spike observed approximately 120 μs after the electric discharge was attributed to both the vaporization of the wire by the electric discharge and the generation of plasma by vaporization of the wire (Sasaki et al. 2011), and the subsequent gradual rise in pressure was due to the deflagration of NM. The effect of the pressure spike on the resultant fracture was found to be negligible. The pressure due to deflagration peaked approximately 130 μs after the pressure spike that corresponds to the electric discharge peak and then decreased. Data were no longer obtained approximately 50 μs after the maximum pressure was attained because of the cutoff of the piezoelectric system. In addition, the inside of the chamber could not be observed after the measurement because of large plastic deformation of the chamber. By conducting preliminary experiment, we obtained the pressure profile in case that the piezoelectric system was cut off. In that case, significant signal errors were observed as irregular and quite steep signal changes. Because the obtained pressure profile in Fig. 3 did not correspond to such case before t = 310 μs and pressure decrease was also successfully captured, it was not considered that the piezoelectric system was cut off before t = 310 μs in Fig. 3.

Although consideration of the lack of reproducibility in the reaction kinetics of deflagration phenomena is generally quite important, we considered that such lack of reproducibility could be minimized in the case of the deflagration of NM due to applied electric discharge under 1500 V and 2500 A, i.e. the condition of very high voltage and high current. Thus, to model the pressure resulting from the deflagration of NM, we used the measured pressure profile in Fig. 3. Considering that the expansion of gaseous products via deflagration can be regarded as a

thermodynamically isentropic process, we applied and extended the Jones–Wilkins–Lee (JWL) equation of state (EOS) (Lee et al. 1973). The JWL EOS has been extensively used to express the isentropic expansion of gaseous products generated by various explosives. In the EOS, a decoupling effect (e.g., Rustan 1998) can also be considered where the pressure acting on the CH dramatically changes with a change in V_{NM}.

It was assumed that the deflagrated volume of NM, $V_d(t)$, increased with elapsed time, that all NM was in the state of deflagration at time t_{peak} after the initiation, and that the maximum pressure was attained at t_{peak}. In other words, by expressing the initial volume of a CH by V_0, $V_d(t)$ became V_0 at $t = t_{peak}$. Considering that NM may have commenced deflagration around the vaporized metal wire installed approximately in the middle of the initiation cartridge vertically, it is reasonable for $V_d(t)$ to be modeled by 2-D expansion with constant propagation velocity; i.e., a quadric function with respect to time. $V_d(t)$ thus has the form

$$V_d(t) = Dt^2 \quad \left(0 \le t \le t_{peak}\right), \qquad (1)$$

where the constant D was determined such that $V_d(t)$ becomes V_0 at $t = t_{peak}$, and a monotonically decreasing function was used for $V_d(t)$ after $t = t_{peak}$. Figure 3 shows that $t_{peak} \sim 130$ μs.

By incorporating $V_d(t)$ into the JWL EOS, the applied pressure $P(t)$ at time t is expressed in the form

$$P(t) = A\exp\left\{-R_1\left(\frac{V(t)}{V_d(t)}\right)\right\} + B\exp\left\{-R_2\left(\frac{V(t)}{V_d(t)}\right)\right\} + C\left(\frac{V(t)}{V_d(t)}\right)^{-(\omega+1)}, \qquad (2)$$

where $V(t)$ is the volume of the expanded gaseous products at time t divided by V_{NM}. The JWL parameters for NM are A = 348.504 GPa, B = 9.021 GPa, C = 1.225 GPa, R_1 = 5.38881, R_2 = 1.39179 and ω = 0.29475, all of which were calculated using the 2003 version of Kihara–Hikita–Tanaka (KHT) code (Tanaka 1985; Tanaka 2003).

2.3. Validation of the pressure model

To investigate the applicability of the proposed pressure model, the pressure profile obtained from Eq. (2) with V_{NM} = 12 mL was compared with the measured pressure in Fig. 3. Because the measurement was conducted inside the chamber

under high pressure, it needs to be interpreted with consideration of the deformation of the chamber. Thus, $P(t)$ was calculated through DFPA (see the next section) assuming deformation of the chamber.

A numerical model for a cross section of the chamber shown in Fig. 2 was employed. Figure 4 shows the 2-D finite element mesh and its size. The cross section was assumed to be perpendicular to the axial direction of the CH in the chamber and to include the initiation cartridge. Linear triangular elements were used. There were 28,292 elements and 14,328 nodal points. All outer boundaries of the mesh were treated as free faces, and $P(t)$ in Eq. (2) was applied to the CH. The physical properties of the chamber used in the analysis were P-wave velocity of 6000 m/s, S-wave velocity of 3100 m/s, density of 8000 kg/m^3, Young's modulus of 200 GPa and Poisson's ratio of 0.3. The analysis was conducted under a plane-strain condition. Tensile fracturing and shear yielding were considered. The onset of yielding was judged using the von Mises criterion. The post-yielding behavior was treated using a perfect elastic–plastic model. Tensile strength and yield strength were 500 and 200 MPa, respectively.

Figure 5 compares the modeled pressure $P(t)$ with measured pressure. Deflagration was considered to commence when the pressure spike due to the electric discharge attained its peak value; i.e., $t = 0$ in Fig. 5. The figure shows good agreement between modeled and measured pressures. Thus, $P(t)$ modeled in this section was applied in the DFPA conducted in Section 4.

3. DFPA

The methodology of DFPA is briefly introduced here. For details, see the literature (Cho 2003; Cho et al. 2008). DFPA is based on a 2-D dynamic FEM and can simulate multiple crack initiations, propagations and coalescences mainly in rocks and rock-like materials such as concrete, while considering material heterogeneity and the size effect. The viscosity of the material is treated using a quality factor, Q (e.g., Kolsky 2012). Tensile and compressive fractures are simulated.

In the case of tensile fracture, different tensile strengths were given to each finite-element boundary such that the strengths satisfied Weibull's distribution (Weibull 1951). Introducing a notion of mean microscopic tensile strength $S_t(V)$ in a given volume V, a cumulative probability function, $G(V, S_t(V))$, is expressed as

$$G(V, S_t(V)) = 1 - \exp\left[\frac{V}{V_{ref}}\left(\frac{S_t(V)}{S_t(V_{ref})}\right)^m \Gamma^m\left(1+\frac{1}{m}\right)\right], \quad (3)$$

where $\Gamma(\cdot)$ is a Gamma function; m, a coefficient of uniformity; V, a volume given by the area of each element having unit thickness in the context of the FEM; V_0, a reference volume; and $S_t(V_{ref})$, the mean microscopic tensile strength in V_{ref}. Random numbers satisfying Eq. (3) were generated to give the spatial distribution of $S_t(V)$ for each finite element. The microscopic tensile strengths on each boundary were calculated by taking the average of its surrounding elements' strengths. Application of Eq. (3) is equivalent to considering material heterogeneity and the size effect of strength characterized by m and the ratio of V to V_{ref}, respectively.

When the calculated tensile stress normally acting on the element boundary exceeded the boundary's tensile strength, crack initiation was expressed by separation of the element boundary. Non-linear behavior in the crack opening was considered and modeled by a tensile softening curve (or cohesive law) (Hillerborg et al. 1976) of a bilinear model (Peterson 1981) illustrated in Fig. 6. The horizontal and vertical axes indicate crack opening displacement, w, and cohesive traction, σ, of each crack, respectively. The area under the w–σ curve is referred to as fracture energy, G_f (Hillerborg et al. 1976). σ_0 is the initial cohesive traction of each crack and equivalent to the element boundary's tensile strength, and w_1 and w_2 correspond to w when $\sigma = (1/4)\sigma_0$ and $\sigma = 0$, respectively.

The compressive fracture in concrete was judged by Mohr–Coulomb criteria for each element because the strain rate corresponding to the deflagration could be regarded as almost quasi-static condition in the literature (Cho et al. 2004) due to the fact that the deflagration is slower phenomena than detonation by one order. The compressive strength of each element was calculated as the product of S_{tb} and the ratio $S_c(V_{ref})/S_t(V_{ref})$, where S_{tb} is the mean value of microscopic tensile strengths of the three boundaries of each element and $S_c(V_{ref})$ is the mean microscopic compressive strength in V_{ref}. After the stress exceeded the Mohr–Coulomb criteria, which relate to the internal friction angle φ and compressive strength of each finite element, the stress state was successively modified to express the plastic strain by applying the opposite sign of the excessive stress from the Mohr–Coulomb envelope to the corresponding finite elements in the next time step.

All DFPAs in the next section were conducted under the plane-strain condition.

4. Investigation of the fracture process in concrete

We investigated the process of fracturing in concrete due to the deflagration of NM. Specifically, controlled splitting of the concrete structure along CHs as shown in Fig. 7 was investigated because it is a representative application of the EDICM. In this case, attaining a flat fracture surface between CHs and minimizing damage to the remaining structure are of particular interest. Field-scale experiments simulating the controlled splitting of concrete were investigated by DPFA.

4.1. Overview of the experiment and analytical conditions of DFPA

Figure 8 is a photograph of a concrete block used in the experiment. The experimental configuration allows application of the EDICM with electric discharge to three CHs. V_{NM} was set to 12 mL and each CH had a diameter of 20 mm and a height of 400 mm. The initiation cartridge was set at the bottom of the CHs, and the remaining upper space in each hole was tamped firmly with silica sand.

Figure 9 shows a 2-D finite element mesh corresponding to the experiment specimen in Fig. 8. The mesh consisted of linear triangular elements and the analyzed plane was assumed to include each CH. There were 146,840 elements, and 74,094 nodal points before the crack initiation. The DFPA applied the interelement crack method and the total number of nodal points thus increased with the progress of fracture. The element size in the mesh was carefully chosen to be small enough to minimize the dependency of the crack path on the mesh. Table 1 shows the physical properties of concrete used in the DFPA. The P-wave velocity was measured and, assuming a Poisson's ratio of 0.20, other elastic constants were calculated according to the theory of elastodynamics. The coefficient of uniformity m was set small enough to express the heterogeneity of concrete. The calculated distribution of the tensile strength over the mesh is shown in Fig. 10. The mean value of the tensile strength was calculated as 13.5 MPa according to the size effect considered in Eq. (3). Although the Q value in the very close vicinity of charge hole was unknown under the extreme condition of the deflagration, we considered that such zone is quite limited (e.g. Cho et al.

2003c; Cho et al. 2004) and the problem could be approximately treated as elastodynamics problem for some distance away from the charge hole. Thus the constant Q was applied. All perimeter boundaries of the mesh were treated as free boundaries. $P(t)$ in Eq. (2) was applied to all CHs. Because the EDICM applies electric discharge, simultaneous initiation was assumed in the DFPA. In addition, considering that the tamped silica sand remained in the CHs after the fracturing and the required time for the fracturing due to the stress wave induced by the deflagration of NM to complete was estimated to be shorter than that for the tamped silica sand to be blown away, the effect of the stemming was not considered in this paper.

4.2. Fracture process in the controlled splitting of concrete

Figure 11 presents the results of DFPA. The figure shows the maximum principal stress distribution and crack propagation. The cold and warm colors show compressive and tensile stresses, respectively. The black lines changing with elapsed time indicate cracks initiated by the applied pressure, $P(t)$. The time t = 0 corresponds to the commencement of the deflagration of NM (see Fig. 5).

Between t = 0 and 40 μs, the stress waves propagated outward from the CHs with their maximum and minimum principle stresses being in the circumferential and radial directions, respectively, as shown in Fig. 12. Around t = 40 μs, cracks initiated around the CHs and propagated in radial directions owing to the circumferential tensile stress, $\sigma_{\theta\theta}(t)$. With time, some of these cracks became predominant and extended toward the outer free faces while remaining cohesive.

Around t = 80 μs, the predominant cracks around each CH reduced in number to 4–6. Additionally, four compressive stress zones (CSZs) formed immediately above and below the middle regions between adjacent CHs where the stress states were in biaxial compression. Then, around t = 100 μs, the intensity of the CSZs increased, leading to the arrest of any crack propagation toward the CSZs. Because the CSZs did not form along the CHs, predominant cracks between CHs extended. In addition, the extension of predominant cracks from CHs 1 and 3 toward the perimeter boundaries continued because these cracks were not affected by the CSZs.

Around t = 160 μs, the crack extensions continued and some predominant cracks between the CHs coalesced as the pressure began to decay after t_{peak} = 130

μs. With the decay of the applied pressure, the CSZs disappeared around t = 160 μs. After crack coalescence between CHs, there was little crack initiation in these regions, and there was only the extension of predominant cracks from CHs 1 and 3 toward the perimeter boundaries. Finally, around t = 240 to 260 μs, these predominant cracks reached the left and right perimeter boundaries, respectively. In addition, the pattern of the open cracks with zero cohesive traction among the predominant cracks showed little change after t = 240 μs. Thus, we consider that the entire fracture pattern resulting from the stress wave was geometrically determined by t = 260 μs, and we stopped the simulation and estimated the final fracture surface; i.e., at t = 260 μs, we extracted the predominant open cracks shown by white dotted lines. In addition, considering that the gaseous products generated by deflagration could selectively flow into these predominant open cracks (Cho 2003), it is reasonable to assume that the predominant open cracks propagating from CHs 1 and 3 could continue to extend as shown by the white dotted arrows, thus forming the final fracture surface.

According to the above estimation of the resultant fracture surface, the region above the fracture surface could remain a concrete mass and the region below could fragment into a few pieces with the help of gas flow. Cracks other than the predominant open cracks are cohesive and thus should be interpreted as damage to the remaining concrete mass.

Because the heterogeneity of concrete could be an important factor affecting the resultant fracture patterns, we conducted three DFPAs to consider the effect of concrete heterogeneity using different spatial strength distributions with the same mean value and variance as the distribution in Fig. 10.

4.3. Comparison of experiment and DFPA results

Figure 13 shows the resultant fracture surface obtained from the experiment (see Fig. 8) and the fracture surfaces predicted in three DFPAs for the different spatial strength distributions. For the DFPA results, predominant open cracks were extracted as white dotted lines and arrows following the same procedure used in the previous subsection and other black lines are cohesive cracks. Next, we mainly focus on the fracture surface between the CHs.

A fracture surface with predominant open cracks connecting CHs was observed in both the experiment and DFPAs. In the three DFPAs conducted to investigate

the heterogeneity of concrete, there was the same trend that fracture surfaces formed between CHs, even though the detail of the fracture geometry was slightly different in each case. Thus, the geometry of the fracture obtained by experiment and that obtained by DFPA were in good agreement. This indicates that the form of the fracture surface connecting CHs could be attained if additional experiments are conducted under the analysed condition.

The above results verify the applicability of our pressure model and demonstrate that the fracture process resulting from the deflagration of NM can be evaluated by DFPA. Thus, the simulation of the fracture process by DFPA could clarify the mechanism of concrete fracture due to the deflagration of NM. We discuss the DFPA result in the following.

4.4. Discussion

In terms of material heterogeneity, it is clear that, even for the same model geometry under the application of the same external force, the fracture pattern depends on the strength distribution. This dependence is due to the difference in positions of crack initiations around the CHs and the difference in the directions of crack growth after the crack initiations depending on the strength heterogeneity of the concrete. Thus, the shapes of fracture surfaces that form between the perimeter boundaries and CH 1 or 3 were completely different in each model. However, the fracture surfaces connecting the CHs were flatter and had only minor shape differences. As described in subsection 4.2, the results can be explained by the formation of CSZs associated with the stress interference and the prevention of crack growth toward them. Thus, if the main aim is to attain a flatter fracture surface along the CHs and avoid crack growth in unexpected directions, there should be smaller spacing between the CHs to minimize the time required for the formation of the CSZs considering that this may be the only measure to control the directions of crack growth. Otherwise, the flatness of the resultant fracture surface between CHs could be compromised. To investigate the validity of this idea, we conducted additional experiments and DFPAs for different spacings between CHs.

Figure 14 shows the fracture patterns for different spacings of CHs. A photograph of the fractured concrete block and the three DFPA results for varying distributions of the material strength are shown. The experimental and DFPA

results clearly agree with each other, demonstrating the applicability of the proposed method. It is seen that the roughness of the fracture surface between the CHs increases with increasing spacing of the CHs. In particular, the flattest surfaces were obtained between CHs in the case presented in Fig. 14(a) with the smallest spacing. In contrast, the roughest surfaces were obtained in the case presented in Fig. 14(b) with the largest spacing owing to the relative delay of formation of CSZs. Hence, the larger spacing leads to a rougher fracture surface because of the greater effect of heterogeneity on the shape of the resultant fracture surface between CHs. In addition, the effect of the free face on the fragmentation size weakens in the loading rate corresponding to the deflagration; i.e., fragmented pieces became larger even for the smallest spacing in Fig. 14(a).

Finally, it is worth mentioning that the result presented in Fig. 14(a) was obtained by applying the proposed pressure modeling method in the case that V_{NM} = 2 mL, using a setup similar to that shown in Fig. 2 and following the same procedure described in Section 2. The value of t_{peak} was also 130 μs in this case. This result indicates that our pressure modeling method is not limited to the particular case discussed in this paper but can account for variation in the volume of deflagration agent.

5. Conclusion

We investigated the mechanism of fracture in concrete due to the deflagration of NM when employing a high-speed splitting technique for rock-like materials (namely, the electric discharge impulse crushing method). For this purpose, we applied dynamic fracture process analysis (DFPA) code based on the 2-D FEM utilizing the interelement crack method. By proposing a new pressure modeling method based on simple pressure measurement and incorporating it into the DFPA, the fracture patterns obtained from several experiments assuming the controlled splitting of concrete along charge holes were found to be expressed well.

In discussion of the fracture process assuming the controlled splitting of concrete due to the deflagration of NM, it was clarified that CSZs formed above and below the middle regions between CHs where maximum and minimum principle stress states were both in compression. These CSZs were found to be essential if flatness of the fracture surface along CHs is the main requirement. It

was also found that smaller spacing between CHs is required for the successful utilization of the CSZs because the time required for the formation of CSZs increases for larger spacing.

Finally, considering the difficulty of both considering the chemical reactions inherent in deflagration of different deflagration agents and calculating the generated pressure, our approach is advantageous in that the generated pressure can be easily expressed according to a simple pressure measurement and application of the JWL equation of state, where the JWL parameters for individual deflagration agents can be readily calculated using, for example, KHT code.

Acknowledgment

The first author appreciates support received in the form of Research Fellowships from the Japan Society for the Promotion of Science for Young Scientists.

References

Abrams DA (1917) Effect of rate of application of load on the compressive strength of concrete. Proc. ASTM 17(2):364–367

Andres U (1989) Parameters of disintegration of rock by electrical pulses. Pow Tech 58:265–269

Bacon L (1962) A method of determining dynamic tensile strength of rock at minimum loading. USBMRI 6067, 22.

Belytschko T, Black T (1999) Elastic crack growth in finite elements with minimal remeshing. Int J Numer Meth Eng 45(5):601–620

Belytschko T, Moës N, Usui S, Parimi C (2001) Arbitrary discontinuities in finite elements. Int J Numer Meth Eng 50(4):993–1013

Bhandari S (1970) Engineer rock blasting operations (1st ed). Taylor & Francis, UK

Birkimer DL (1970) A possible fracture criterion for the dynamic tensile strength of rock. Proc. 12th Symposium on Rock Mechanics, Rolla, Missouri, 573–590

Bluhm H, Frey W, Giese H, Hoppe P, Schultheiss C, Strassner R (2000) Application of pulsed HV discharges to material fragmentation and recycling. IEEE Trans Dielect Elect Insul 7(5):625–636

Borovikov VA, Vanyagin I F (1995) Modelling the Effects of Blasting on Rock Breakage. Taylor & Francis, UK

Brara A, Camborde F, Klepacxko JR, Mariotti C (2001) Experimental and numerical study of concrete at high strain rates in tension. Mech Mater 33(1):33–45

Bulson PS (1997) Explosive loading of engineering structures. Taylor & Francis, UK

Camacho GT, Ortiz M (1996) Computational modeling of impact damage in brittle materials. Int J Solids Struct 33:2899–2938

Carol I, Prat PC, Lopez CM (1997) Normal/shear cracking model: Application to discrete crack analysis. J Eng Mech 123(8):765–773

Cho SH (2003a) Dynamic fracture process analysis of rock and its application to fragmentation control in blasting. Dissertation, Hokkaido University

Cho SH, Ogata Y, Katsuhiko K (2003b) Strain rate dependency of the dynamic tensile strength of rock. Int J Rock Mech Min Sci 40(5):763–777

Cho SH, Nishi M, Yamamoto M, Kaneko K (2003c) Fragment Size Distribution in Blasting. Materials Transactions 44(5): 951–956

Cho SH, Kaneko K (2004) Influence of the applied pressure waveform on the dynamic fracture processes in rock. Int J Rock Mech Min Sci, 41(5):771–784

Cho SH, Mohanty B, Ito M, Nakamiya Y, Owada S, Kubota S, Ogata Y, Tsubayama A, Yokota M, Kaneko K (2006) Dynamic Fragmentation of Rock by High-Voltage Pulses. Proc 41st U.S. Symposium on Rock Mechanics, Curran Associates, Inc., 06-1118

Cho SH, Nakamura Y, Mohanty B, Yang HS, Kaneko K (2008) Numerical study of fracture plane control in laboratory-scale blasting. Eng Fract Mech 75(13):3966–3984

Gálvez JC, Cervenka J, Cendón DA, Saoumad V (2002) A discrete crack approach to normal/shear cracking of concrete. Cem Conc Res 32:1567–1585

Grote DL, Park SW, Zhou M (2001) Dynamic behavior of concrete at high strain rates and pressures: I. experimental characterization. Int J Impact Eng 25:869–886

Hallquist JO (1998) LS-DYNA theory manual. Livemore Software Technology Corporation, USA

Hanchak SJ, Forrestal MJ, Young ER, Erhrgott JQ (1992) Perforation of concrete slabs with 48 MPa (7 ksi) and 140 MPa (20 ksi) unconfined compressive strengths. Int J Impact Eng 12:1–7

Hillerborg A, Modeer M, Petersson PE (1976) Analysis of crack formation and crack growth in concrete by means of fracture mechanics and finite elements. Cem Conc Res 6(6):773–781

Hofmann J and Weisse THGG (1997) Pulsed power technologies for commercial materials reduction and crushing applications. Proc. 11th IEEE International Pulsed Power Conference, 203–207

Kaneko K, Matsunaga Y, Yamamoto M (1995) Fracture mechanics analysis of fragmentation process in rock blasting. Kayaku Gakkaishi 56:207–215 (in Japanese with English abstract)

Kolsky H (2012) Stress waves in solids (2nd ed). Dover Publications, New York

Lee E, Finger M, Collins W (1973) JWL equation of state coefficients for high explosives. Lawrence Livermore National Laboratory, Livermore, CA, Rept-UCID-16189

Lisitsyn IV, Inoue H, Katsuki S, Akiyama H, Nishizawa I (1999) Drilling and Demolition of Rocks by Pulsed Power. Proc 12th IEEE International Pulsed Power Conference Vol. 1, 169–172

Malvern LE, Jenkins DA, Tang T, Ross CA (1985) Dynamic compressive testing of concrete. Proc 2nd Symposium on the Interaction of Non-Nuclear Munitions with Structures, Florida, USA, 194–199

Moës N, Dolbow J, Belytschko T (1999) A finite element method for crack growth without remeshing. Int J Numer Meth Eng, 46:131–150

Narahara S, Namihira T, Nakashima K, Inoue S, Iizasa S, Maeda S, Shigeishi M, Ohtsu M, Akiyama H (2007) Evaluation of concrete made from recycled coarse aggregates by pulsed power discharge. Proc 16th IEEE International Pulsed Power Conference, Vol. 1, 748–751

Ortiz M, Pandolfi A (1999) Finite-deformation irreversible cohesive elements for three-dimensional crack-propagation analysis. Int J Num Meth Eng 44:1267–1282

Peterson P E (1981) Crack growth and development of fracture zones in plain concrete and similar materials. Lund Institute of Technology, Lund. Report TVBM-100

Rinehardt JS (1965) Dynamic fracture strength of rocks. Proc 7th Symposium on Rock Mechanics, New York, American Institute of Mining, 205–208

Rim GH, Cho CH, Lee HS, Pavlov EP (1999) An electric-blast system for rock fragmentation. Proc 12th IEEE International Pulsed Power Conference, Vol. 1, 165–168

Ross CA, Tedesco JW, Kuennen ST (1995) Effects of strain rate on concrete strength. ACI Mater J 92:37–47

Rossi P (1991) A physical phenomena which can explain the mechanical behavior of concrete under high strain rates. Mater Struct 24:422–4

Ruiz G, Ortiz M, Pandolfi A (2000) Three-dimensional finite-element simulation of the dynamic Brazilian tests on concrete cylinders. Int J Numer Meth Eng 48:963–994

Rustan A (1998) Rock blasting terms and symbols: a dictionary of symbols and terms in rock blasting and related areas like drilling, mining and rock mechanics. Taylor & Francis, UK

Sasaki K, Kitajima H, Maehata H, Sakamoto R, Kubota S (2011) Development of splitting technology by using electric discharge impulse crushing system. 37th Annual Conference on Explosives & Blasting Technique, 301–311

Segura JM, Carol I (2010) Numerical modelling of pressurized fracture evolution in concrete using zero-thickness interface elements. Eng Fract Mech 77:1386–1399

Shao P, Sheng P, Zhou JS, Long JK, Wu YQ (2010) Applying high voltage pulse discharge in rock blasting: Theoretical problems. 2nd International Conference on Computer Engineering and Technology (ICCET), Vol. 5, 349–353

Song JH, Wang H, Belytschko T (2008) A comparative study on finite element methods for dynamic fracture. Comput Mech 42:239–250

Song JH, Belytschko T (2009) Cracking node method for dynamic fracture with finite elements. Int J Numer Meth Eng 77:360–385

Stiehr JF and Dean JL (2011) ISEE blasters' handbook (18th ed.). International Society of Explosives, Cleveland

Stolarska M, Chopp DL, Moës N, Belytschko T (2001) Modeling crack growth by level sets in the extended finite element method. Int J Numer Meth Eng 51:943–960

Tanaka K (1985) Detonation properties of high explosives calculated by revised Kihara–Hikita equation of state. Proc 8th Symposium (International) on Detonation, 548–557

Tanaka K (2003) Detonation properties of condensed materials (KHT 2003). http://riodb.ibase.aist.go.jp/ChemTherm/kht_e.htm. Accessed 28 August 2012

Weibull W (1951) A statistical distribution function of wide applicability. J Appl Mech 18:293–297

Weise THGG and Loffler JM (1993) Experimental investigations on rock fractioning by replacing explosives with electrically generated pressure pulses. Proc 9th IEEE International Pulsed Power Conference, Digest of Technical papers, Vol. 1, 19–22

Xu XP, Needleman A (1994) Numerical simulation of fast crack growth in brittle solids. J Mech Phys Solids 42:1397–1434

Yamamoto M, Ichijo T, Inaba T, Morooka K, Kaneko K (1999) Experimental and theoretical study on smooth blasting with electronic delay detonators. Fragblast 3(1):3–24

Zhang ZX, Kou SQ, Jiang LG, Lindqvist PA (2000) Effects of loading rate on rock fracture: fracture characteristics and energy partitioning. Int J Rock Mech Min Sci 37:745–762

Title of Table

Table 1 Physical properties of concrete used in DFPA.

Figure captions

Fig. 1 Schematic diagram of the initiation cartridge used in the EDICM.

Fig. 2 Schematic diagram (left) and photograph (right) of the pressure measurement using a stainless steel chamber; the volume of NM was 12 mL.

Fig. 3 Measured pressure profile.

Fig. 4 2-D finite element mesh for a single cross section of the chamber.

Fig. 5 Comparison of measured and modeled pressures.

Fig. 6 Tensile softening curve used in DFPA (bilinear model).

Fig. 7 Schematic diagram of the controlled splitting of a concrete structure along charge holes.

Fig. 8 Concrete block before the application of EDICM.

Fig. 9 Finite element mesh used in the analysis of the concrete block in Fig. 8.

Fig. 10 Distribution of the microscopic tensile strength obtained from Eq. (3).

Fig. 11 Result of the fracture process simulated by DFPA for chosen time steps.

Fig. 12 Temporal change in radial and circumferential stress components on the wall of a CH before crack initiation.

Fig. 13 Photograph of a fractured specimen and fracture surfaces predicted by DFPAs.

Fig. 14 Experimentally and numerically obtained fracture patterns.

(a) The case for spacing of 80 mm.

(b) The case for spacing of 600 mm.

Tables

Table 1. Physical properties of concrete used in DFPA.

P-wave velocity, V_p (m/s)	4000
S-wave velocity, V_s (m/s)	2450
Density, ρ (kg /m^3)	2200
Elastic modulus, E (GPa)	31.7
Poisson's ratio, v (–)	0.2
Fracture energy, G_f (Pa m)	75
Quality factor, Q (–)	10
Mean microscopic tensile strength in reference volume, $S_t(V_{ref})$ (MPa)	3
Mean microscopic compressive strength in reference volume, $S_c(V_{ref})$ (MPa)	45
Reference volume, V_{ref} (m^3)	7.8×10^{-5}
Coefficient of uniformity, m (–)	5
Internal friction angle, φ (degree)	50

Figure1

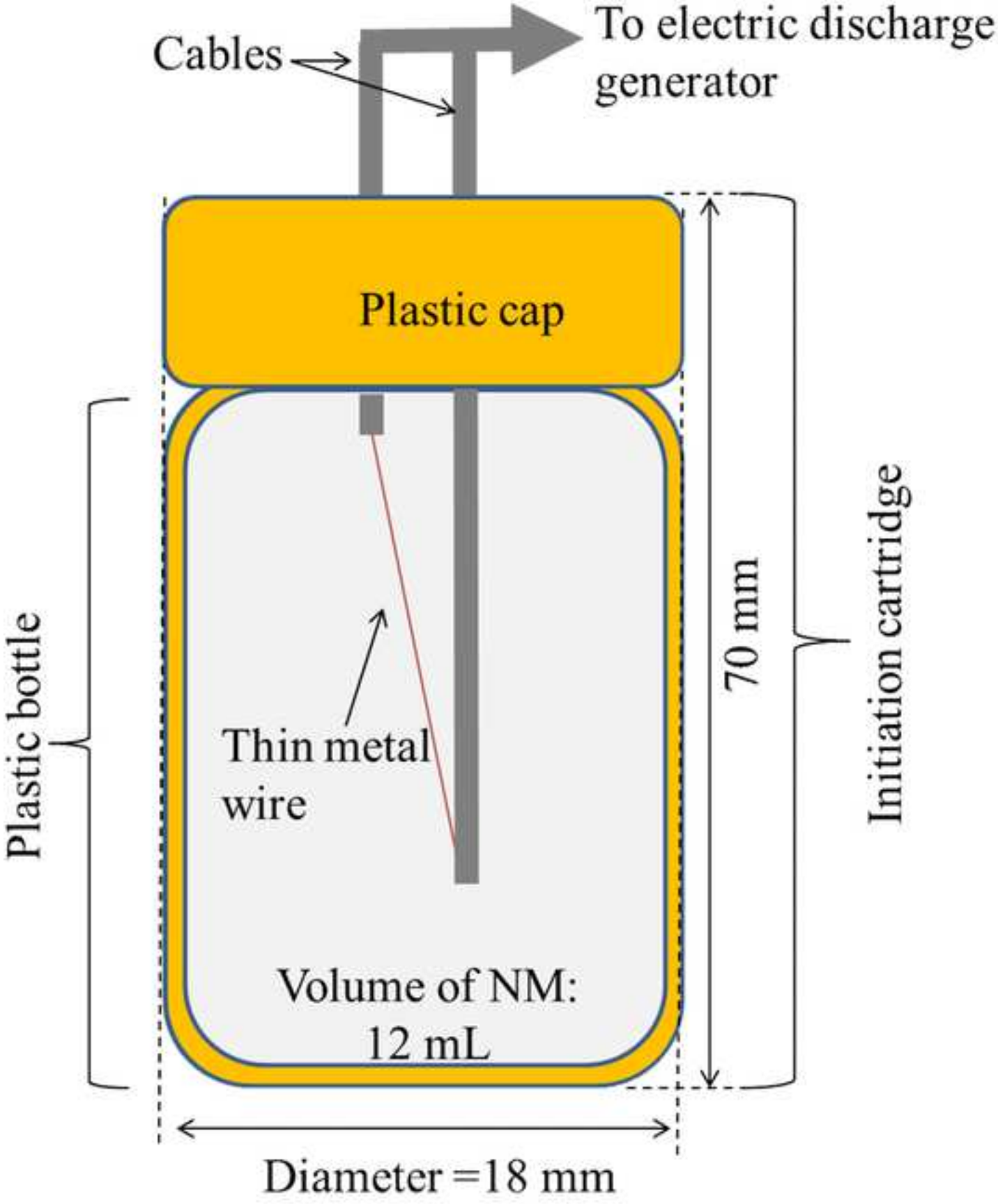
Cables
To electric discharge generator
Plastic cap
Plastic bottle
Thin metal wire
Volume of NM: 12 mL
70 mm
Initiation cartridge
Diameter =18 mm

Figure2

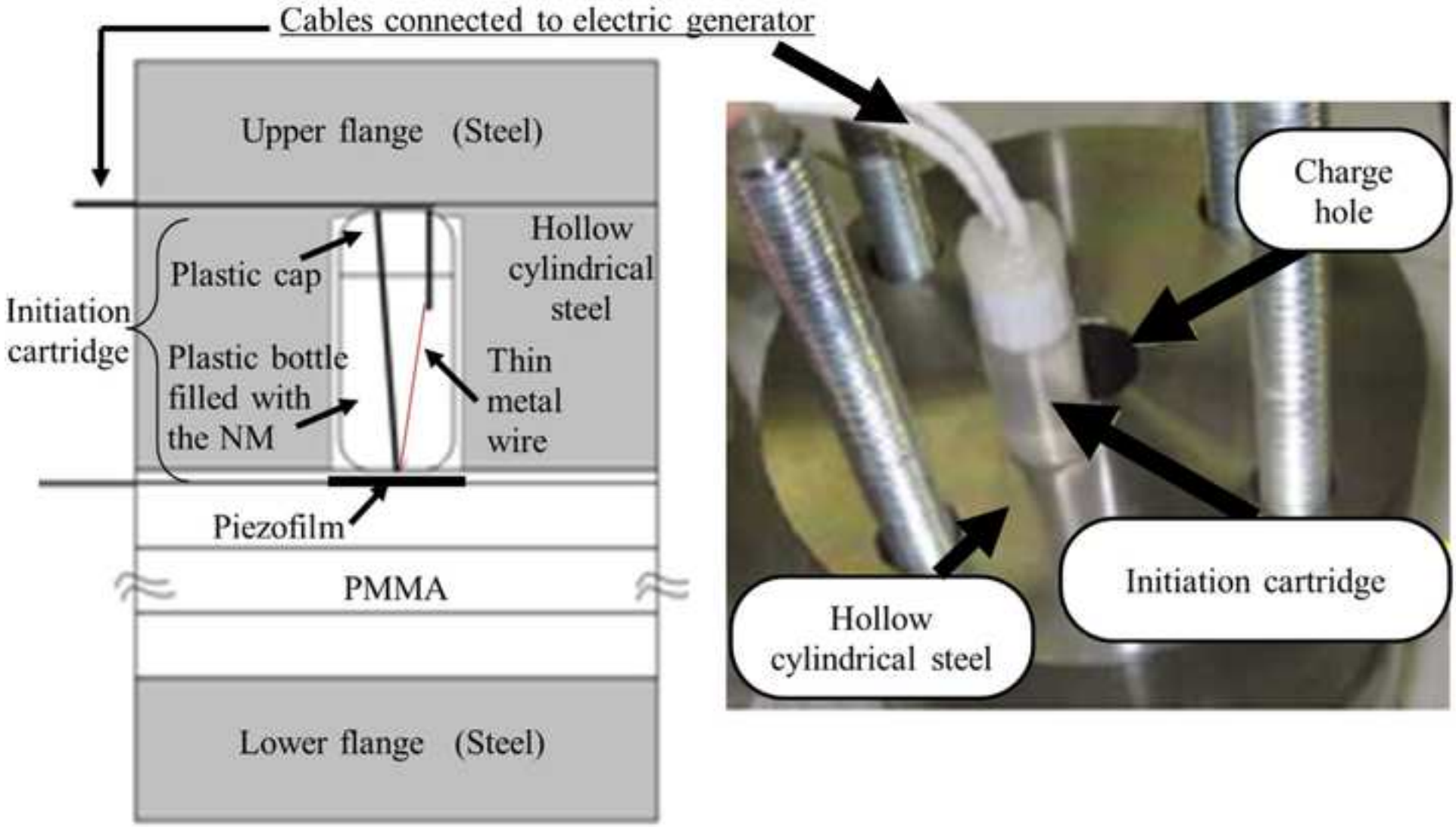
Cables connected to electric generator
Upper flange (Steel)
Hollow cylindrical steel
Plastic cap
Initiation cartridge
Plastic bottle filled with the NM
Thin metal wire
Piezofilm
PMMA
Lower flange (Steel)
Charge hole
Initiation cartridge
Hollow cylindrical steel

Figure3

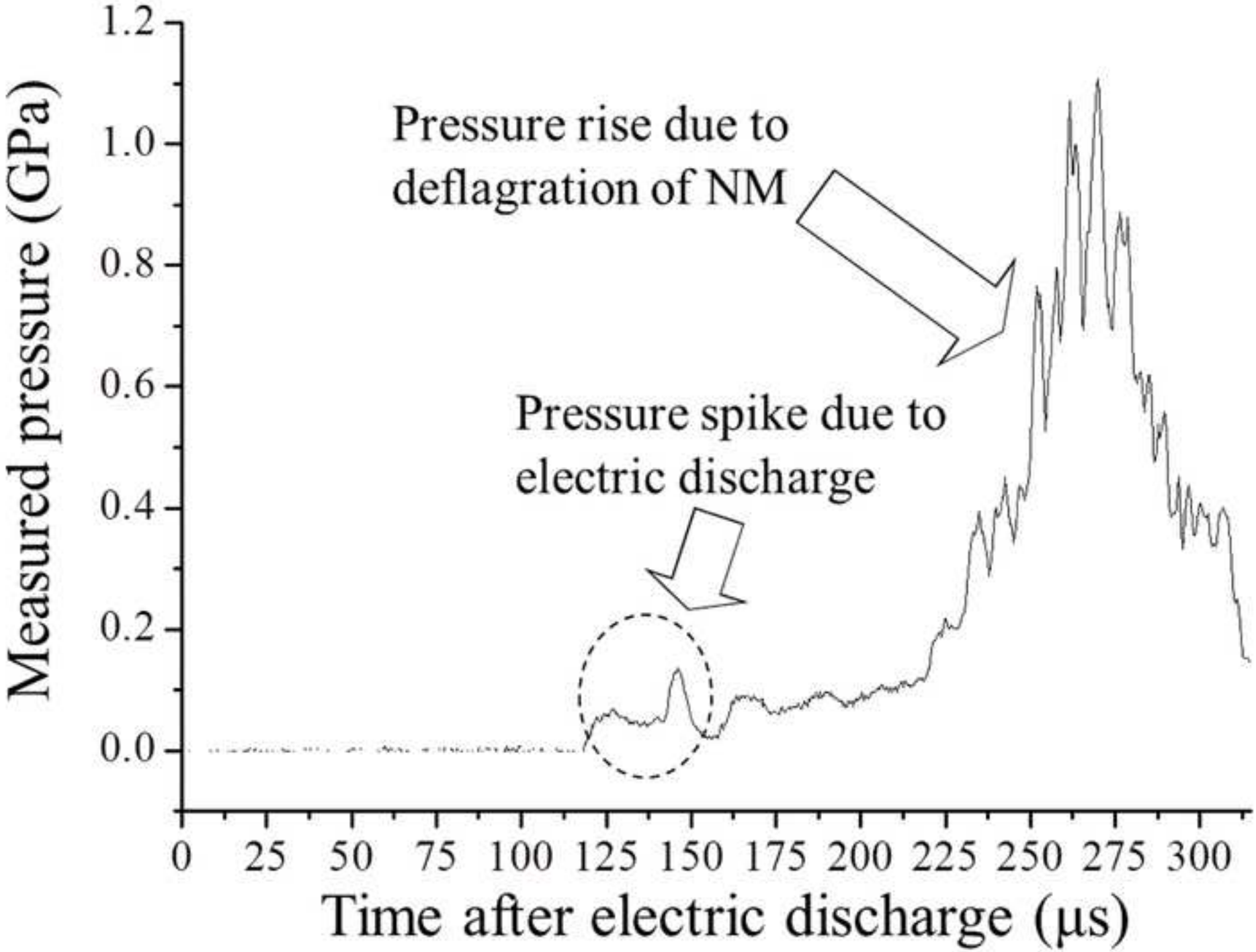
Measured pressure (GPa)
1.2
1.0
0.8
0.6
0.4
0.2
0.0
Pressure rise due to
deflagration of NM
Pressure spike due to
electric discharge
0
25
50
75
100
125
150
175
200
225
250
275
300
Time after electric discharge (μs)

Figure4

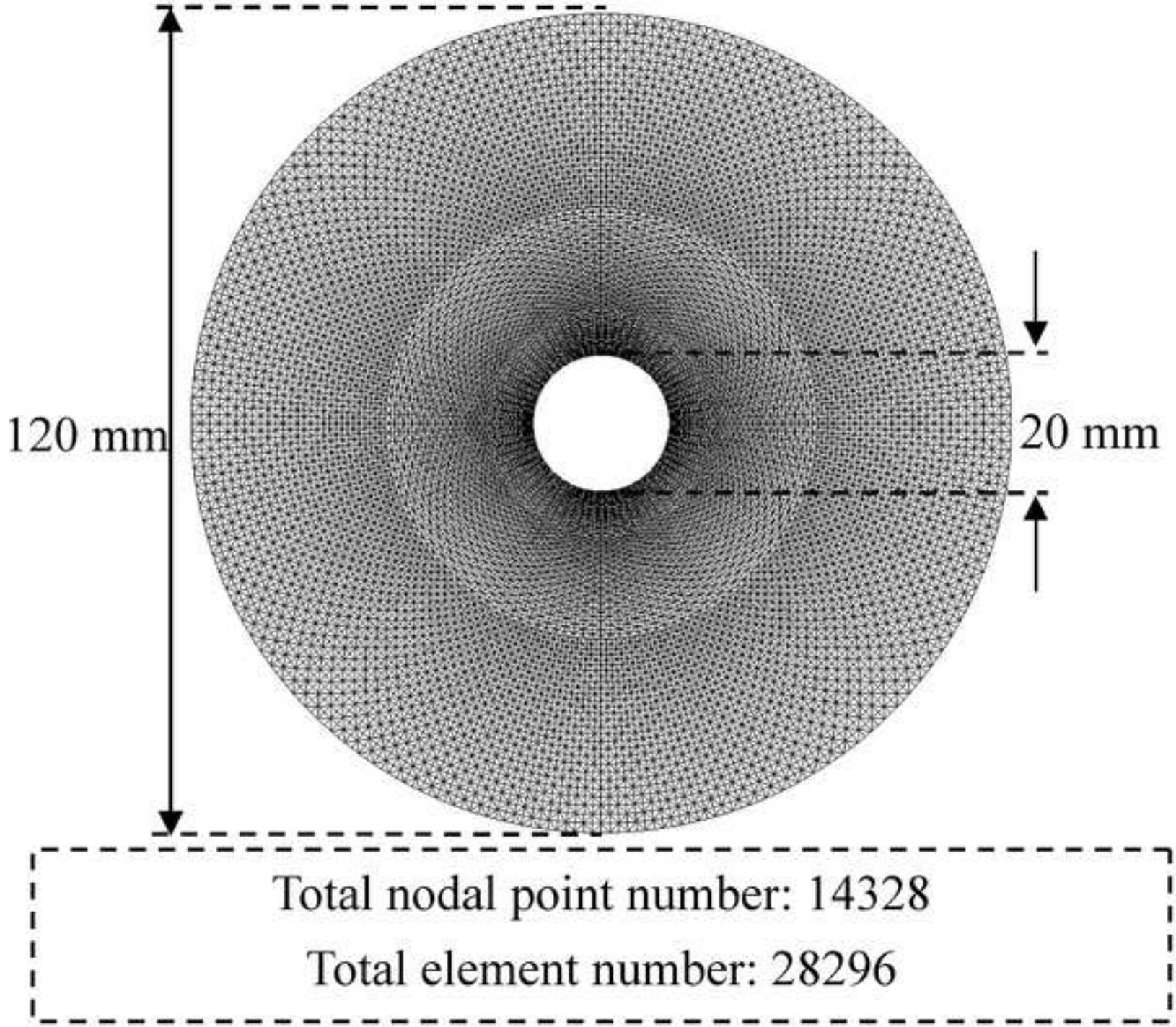
120 mm
20 mm
Total nodal point number: 14328
Total element number: 28296

Figure5

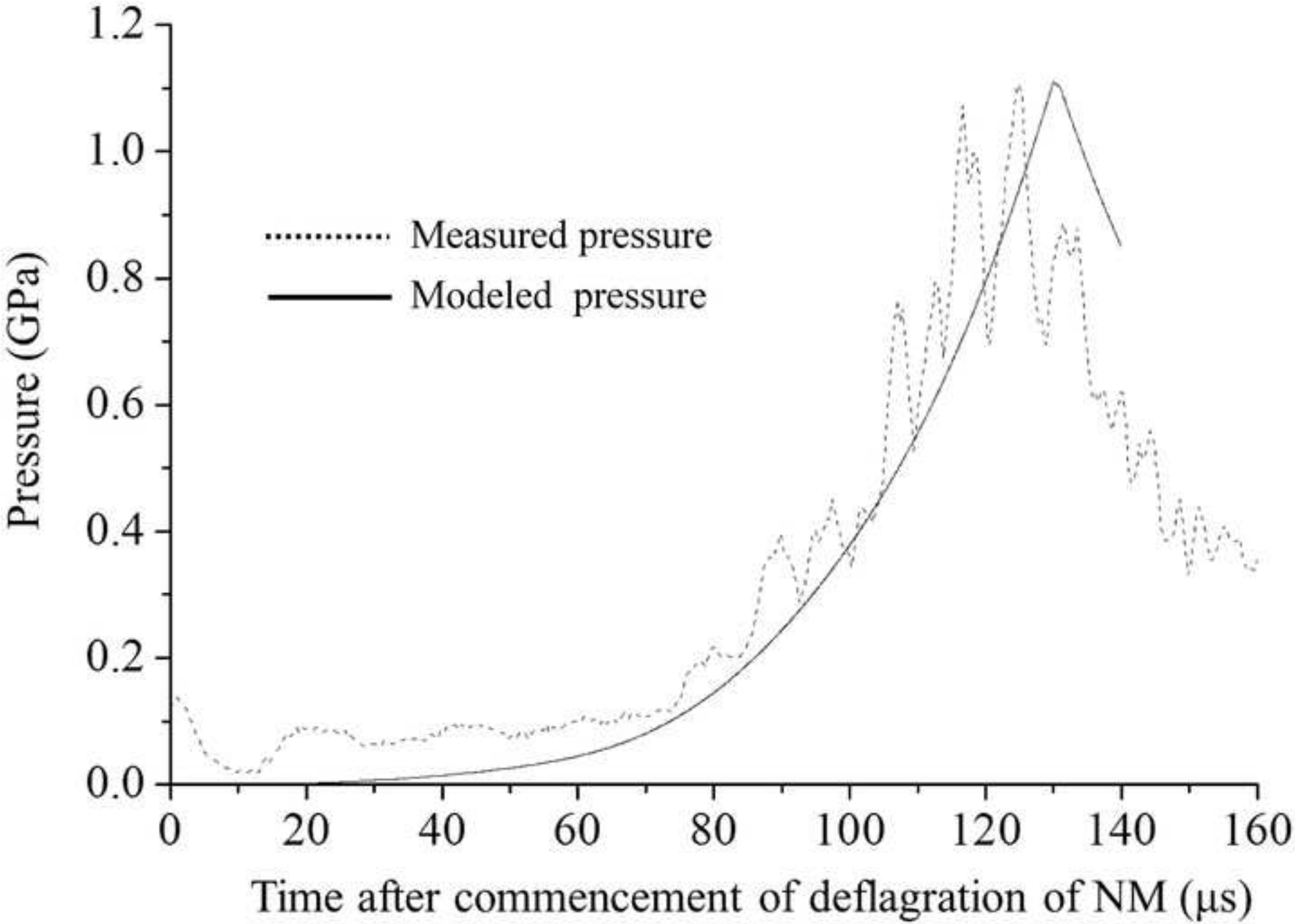
Measured pressure
Modeled pressure
Pressure (GPa)
1.2
1.0
0.8
0.6
0.4
0.2
0.0
0
20
40
60
80
100
120
140
160
Time after commencement of deflagration of NM (μs)

Figure6

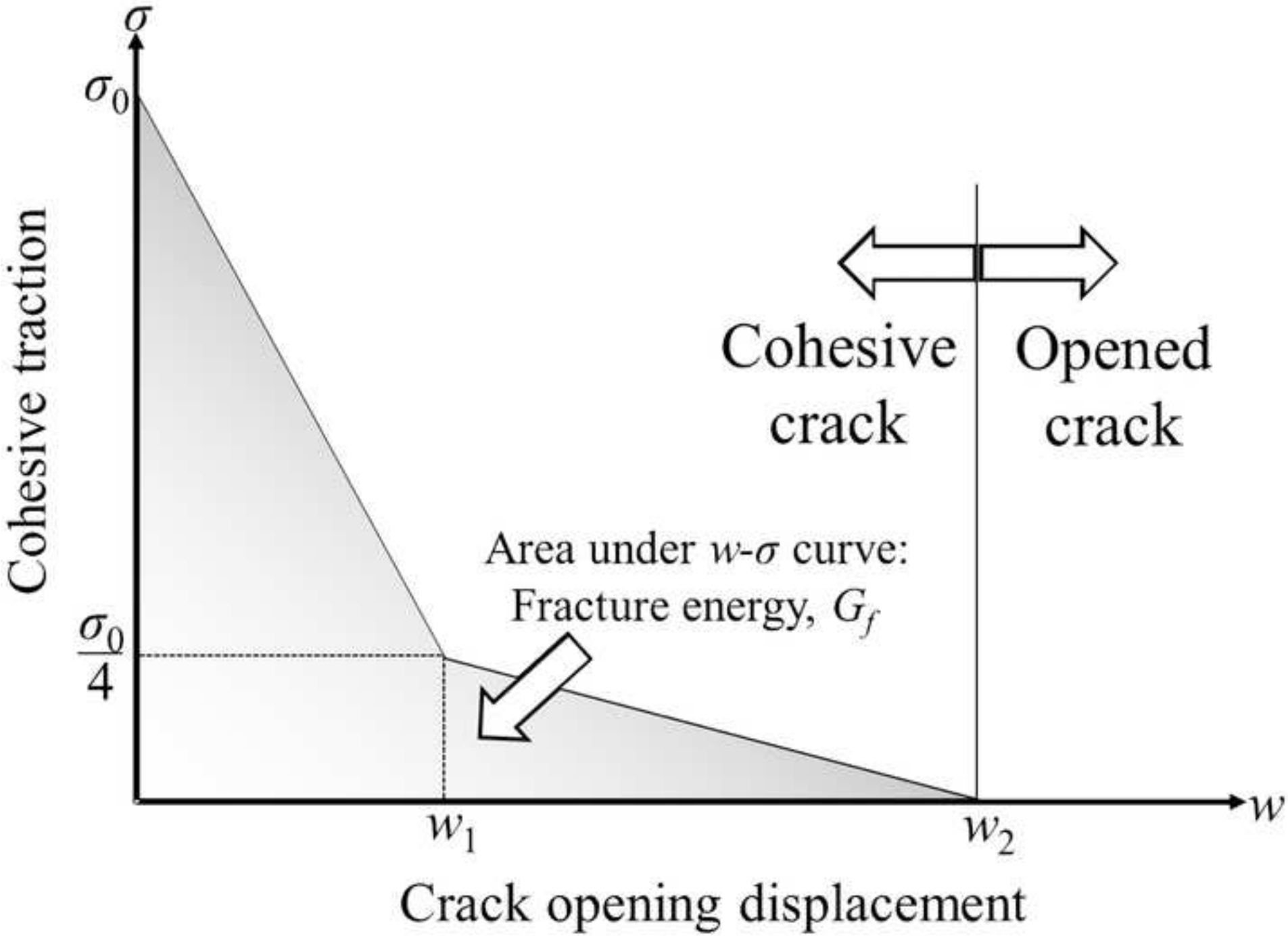
σ
σ0
Cohesive traction
σ0/4
Cohesive crack
Opened crack
Area under w-σ curve:
Fracture energy, Gf
w1
w2
w
Crack opening displacement

Figure7

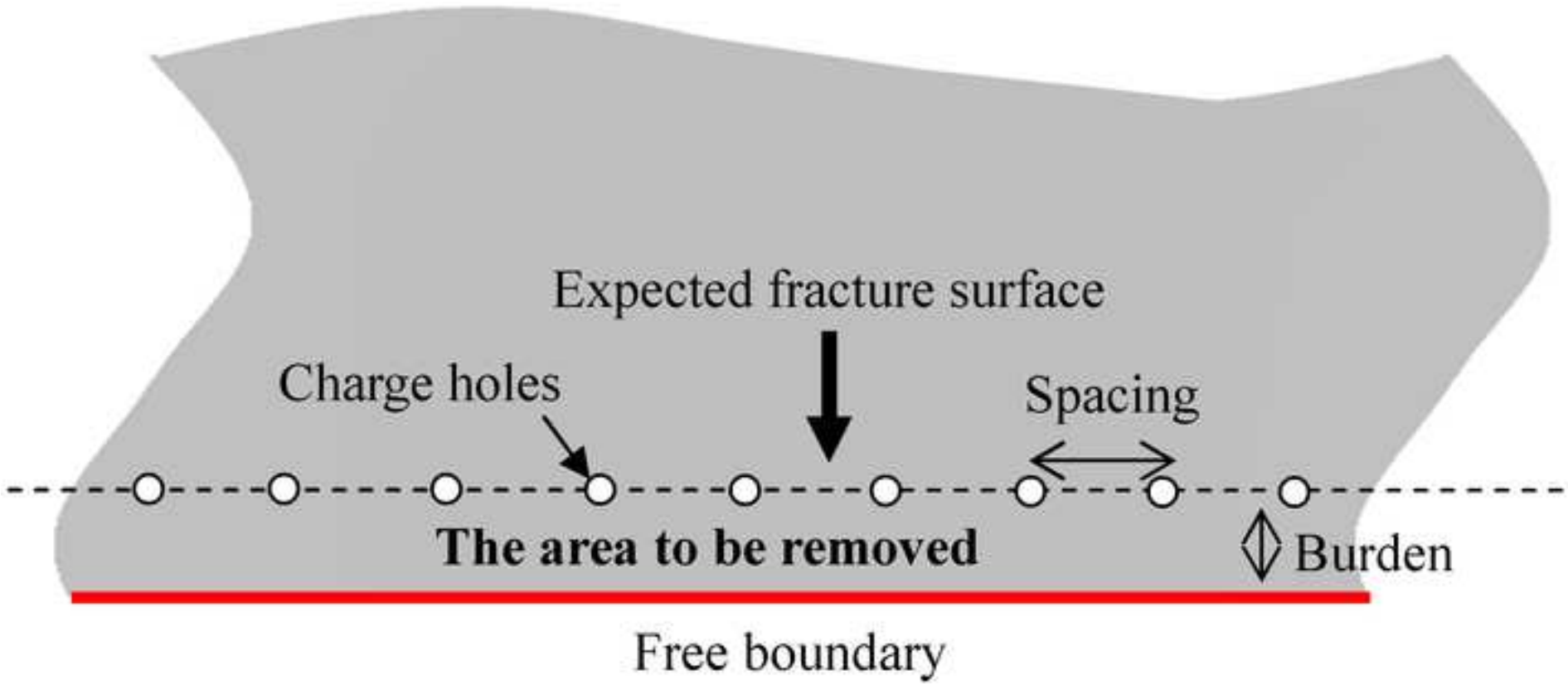
Expected fracture surface
Charge holes
Spacing
The area to be removed
Burden
Free boundary

Figure8

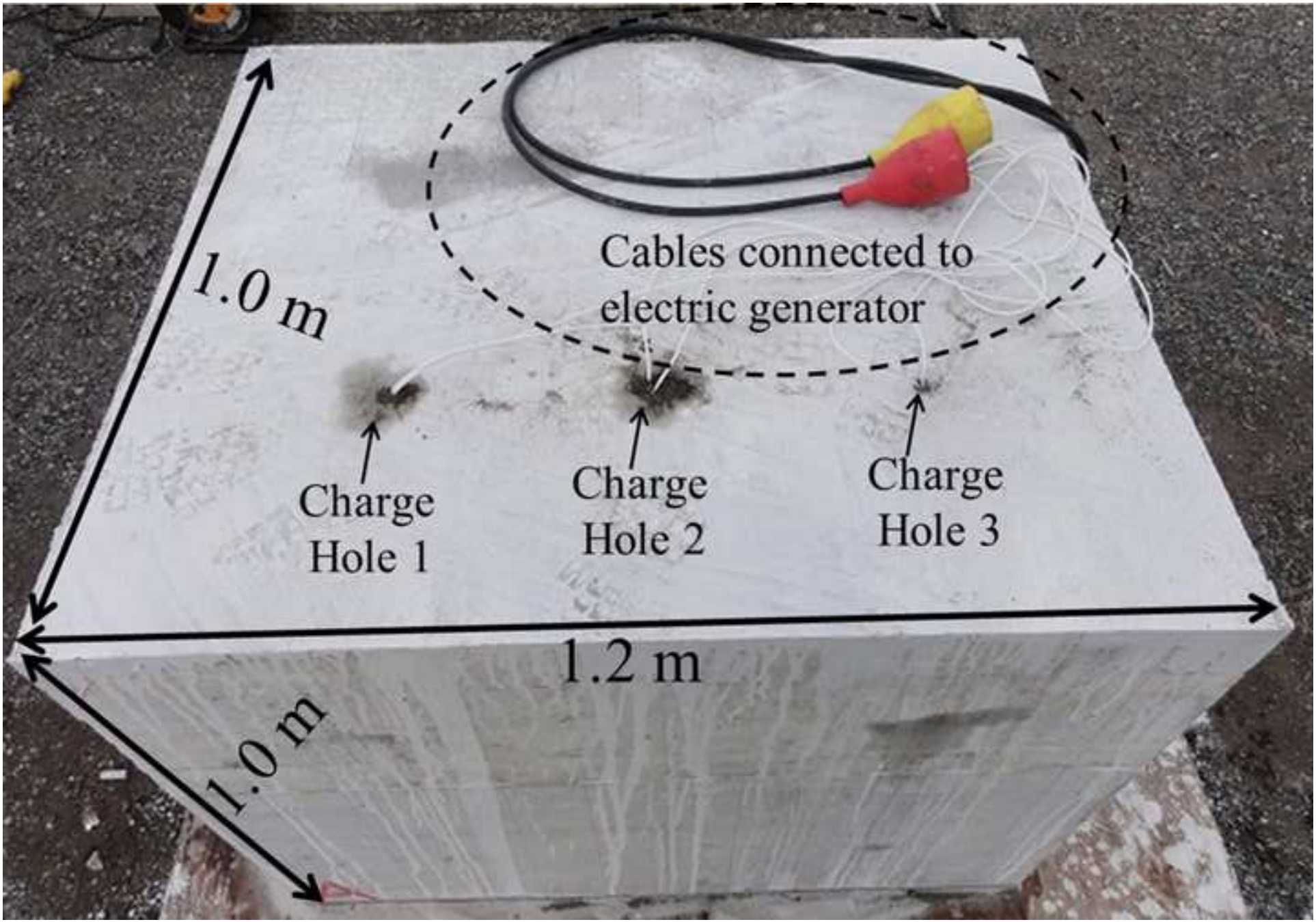
1.0 m
Cables connected to
electric generator
Charge
Hole 1
Charge
Hole 2
Charge
Hole 3
1.2 m
1.0 m

Figure9

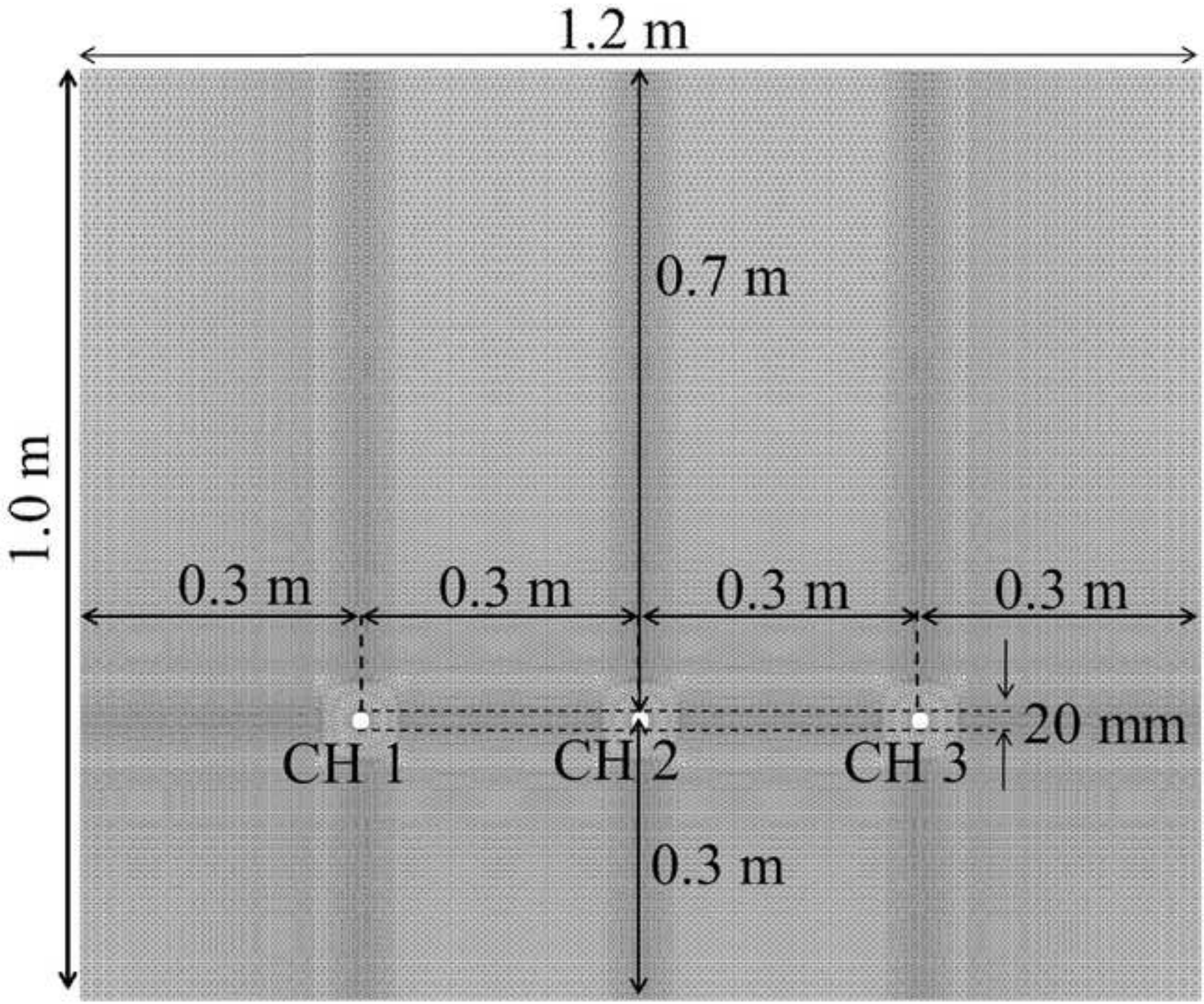

Figure10

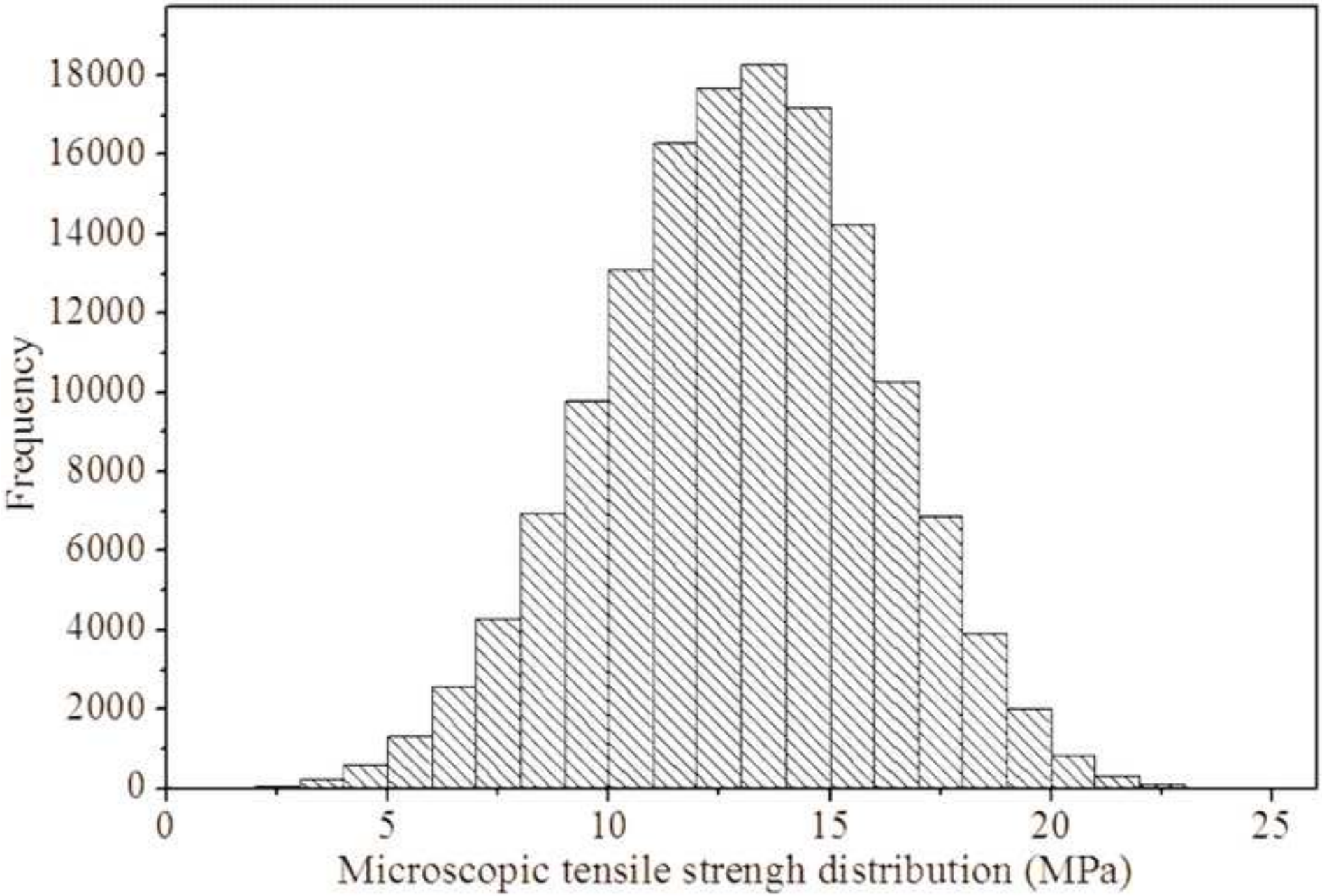
Frequency
18000
16000
14000
12000
10000
8000
6000
4000
2000
0
0
5
10
15
20
25
Microscopic tensile strengh distribution (MPa)

Figure11

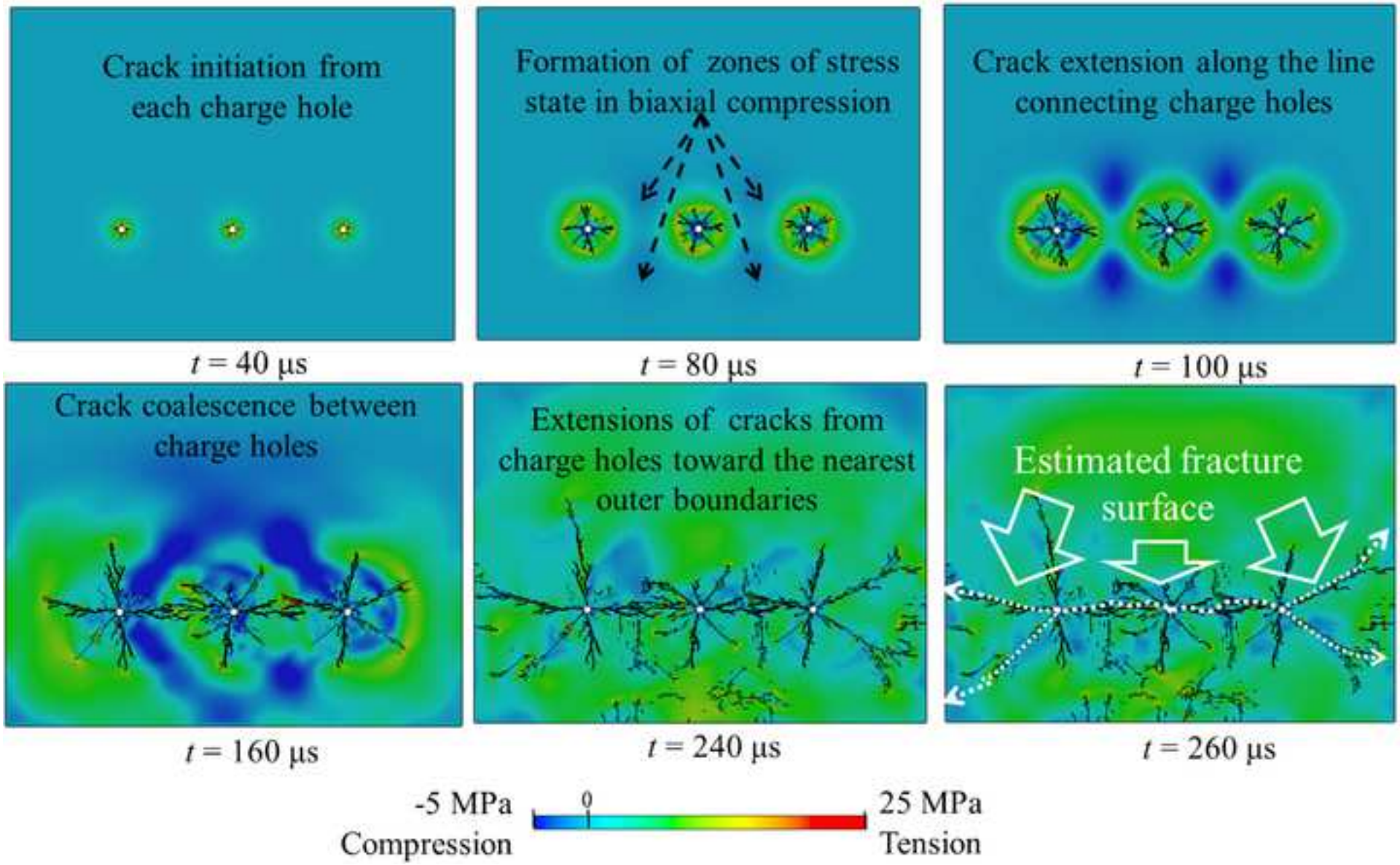
Crack initiation from each charge hole
t = 40 μs
Formation of zones of stress state in biaxial compression
t = 80 μs
Crack extension along the line connecting charge holes
t = 100 μs
Crack coalescence between charge holes
t = 160 μs
Extensions of cracks from charge holes toward the nearest outer boundaries
t = 240 μs
Estimated fracture surface
t = 260 μs
-5 MPa
Compression
0
25 MPa
Tension

Figure12

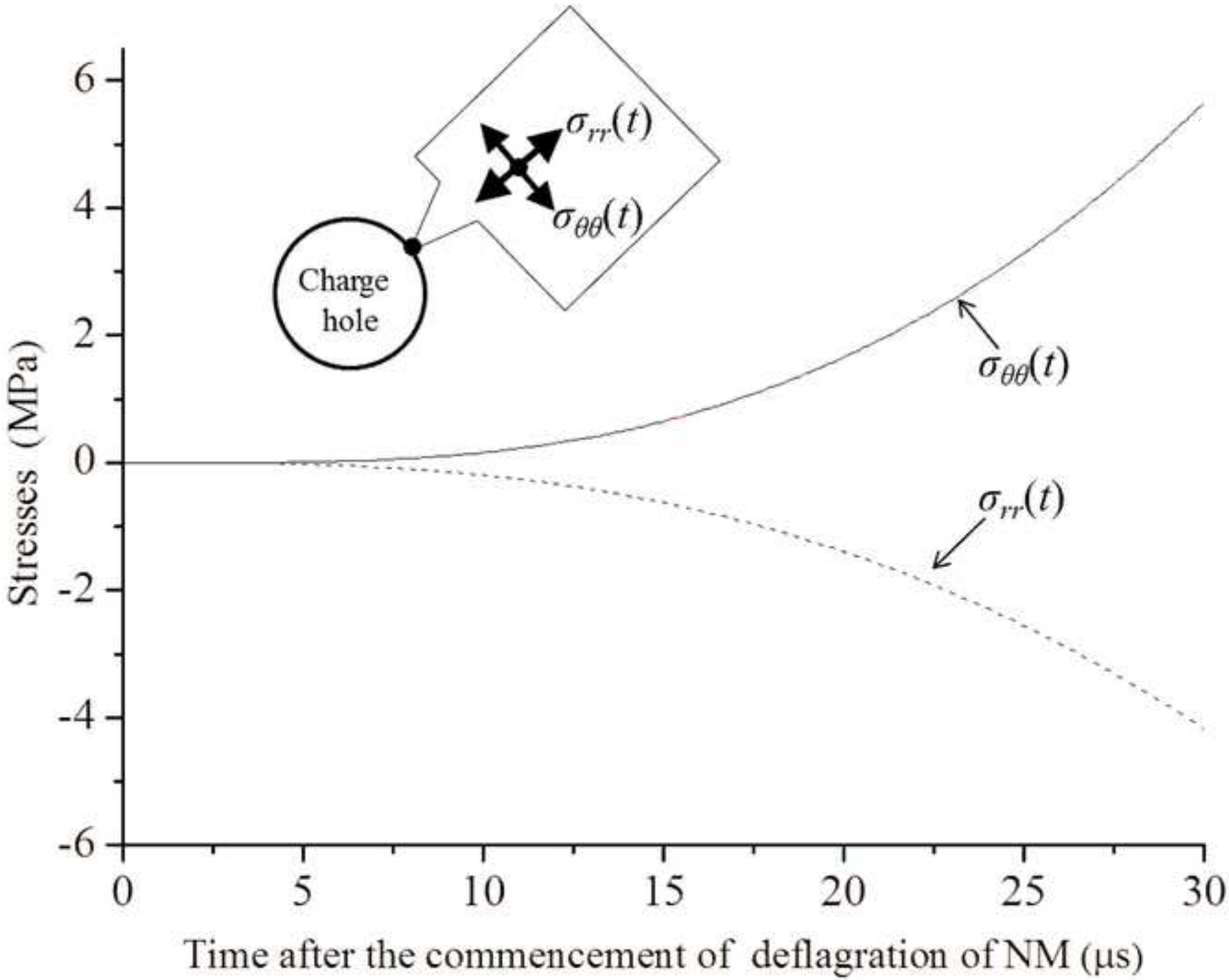
Charge hole
$\sigma_{rr}(t)$
$\sigma_{\theta\theta}(t)$
$\sigma_{\theta\theta}(t)$
$\sigma_{rr}(t)$
Stresses (MPa)
6
4
2
0
-2
-4
-6
0
5
10
15
20
25
30
Time after the commencement of deflagration of NM (μs)

Figure13

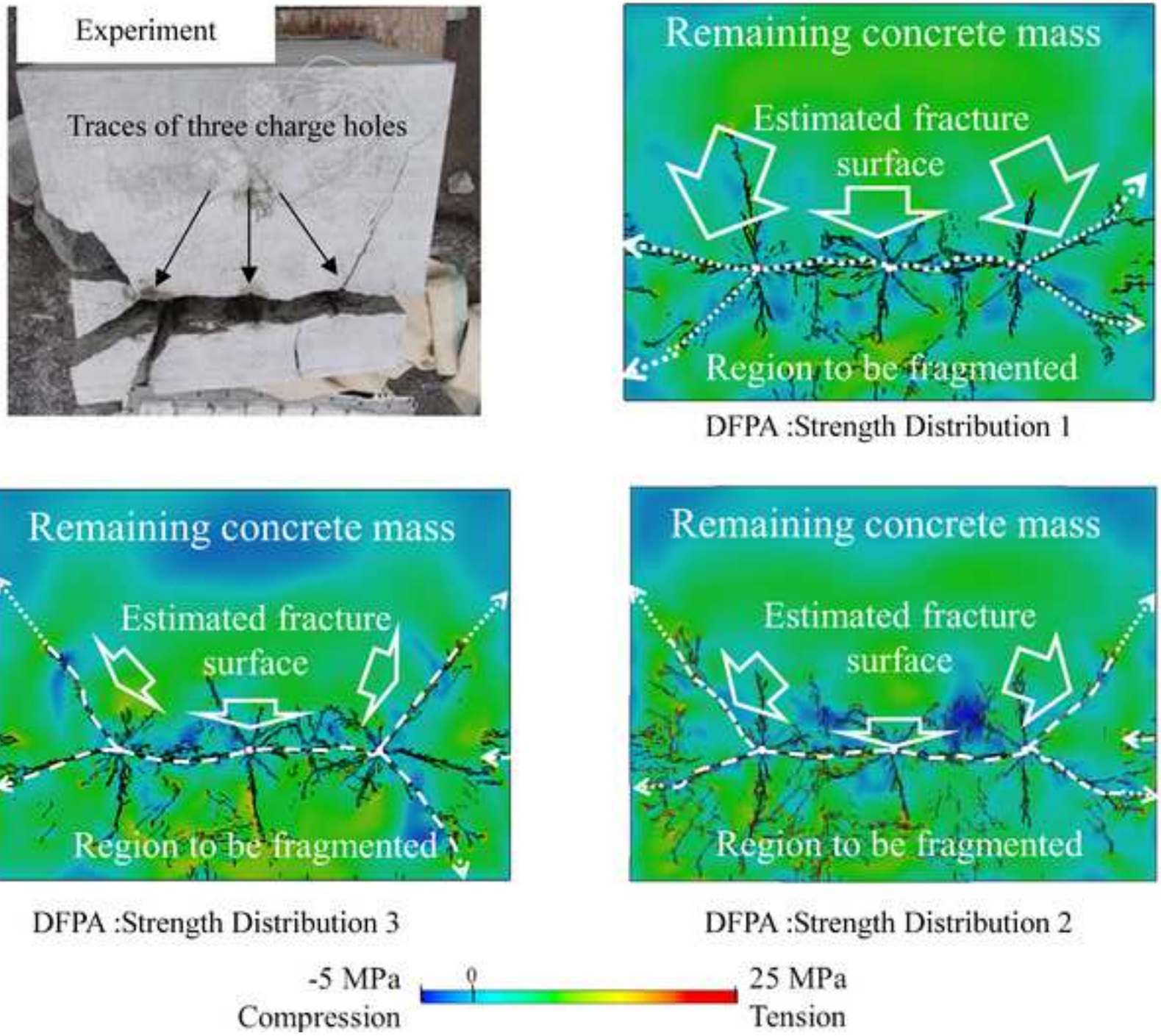
Experiment
Traces of three charge holes
Remaining concrete mass
Estimated fracture surface
Region to be fragmented
DFPA :Strength Distribution 1
Remaining concrete mass
Estimated fracture surface
Region to be fragmented
DFPA :Strength Distribution 3
Remaining concrete mass
Estimated fracture surface
Region to be fragmented
DFPA :Strength Distribution 2
-5 MPa
Compression
0
25 MPa
Tension

Figure14(a)

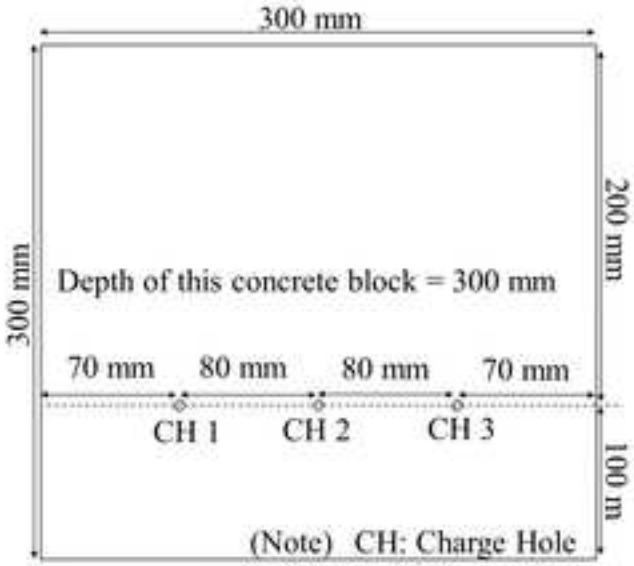

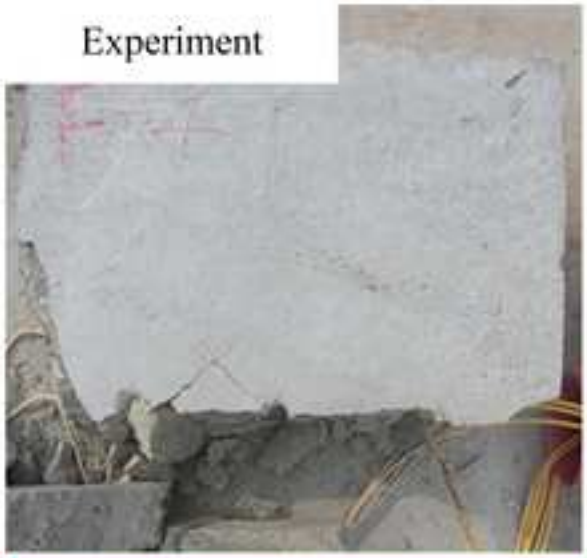

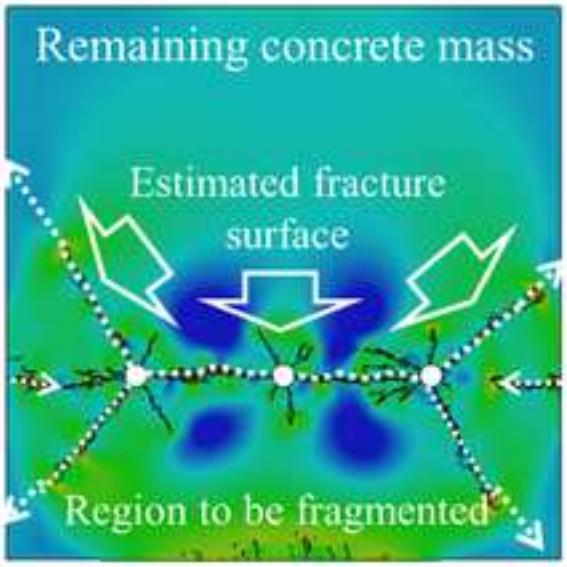

DFPA :Strength Distribution 1

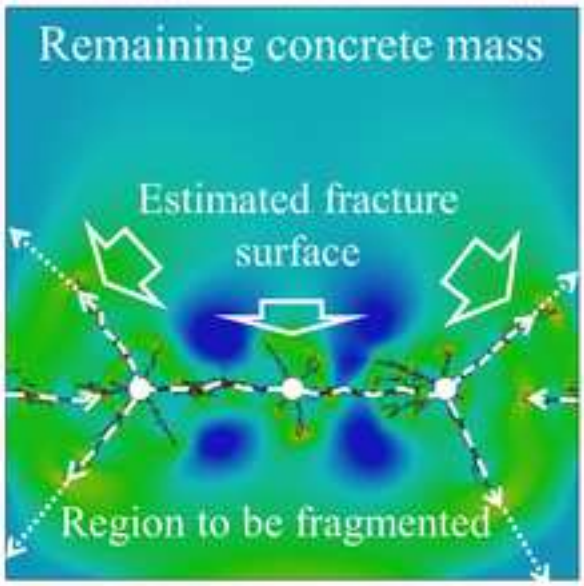

DFPA : Strength Distribution 2

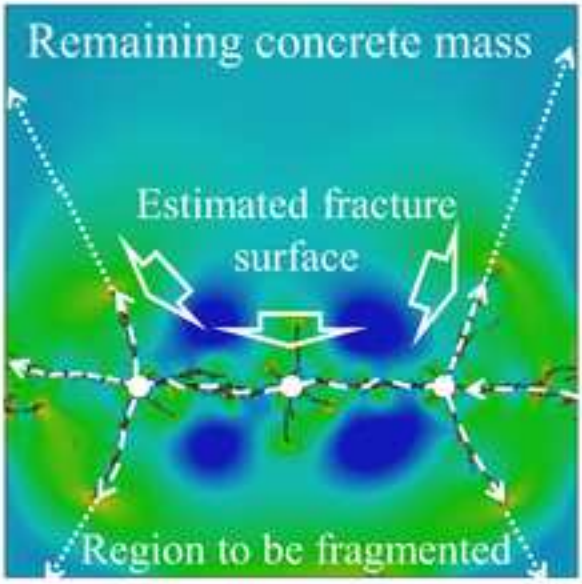

DFPA :Strength Distribution 3

The results of DFPAs are t = 110 μs.

V_{NM} = 2 mL.

Figure14(b)

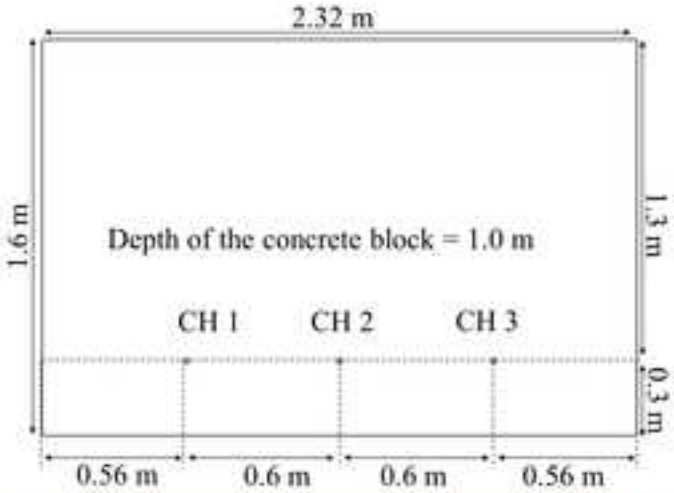

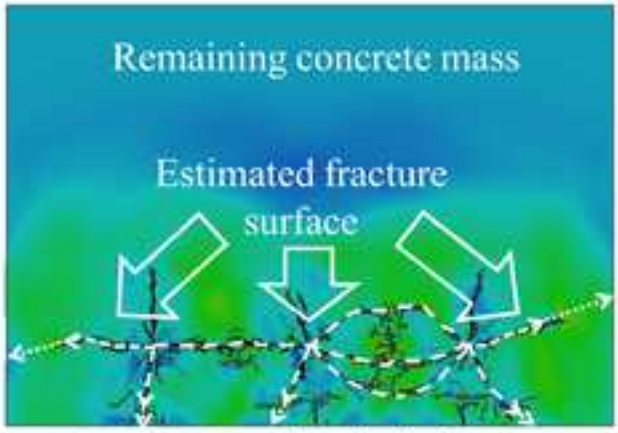

DFPA: Strength Distribution 1

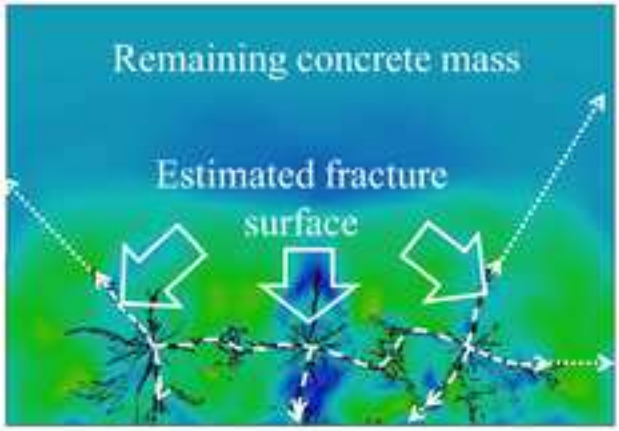

DFPA: Strength Distribution 2

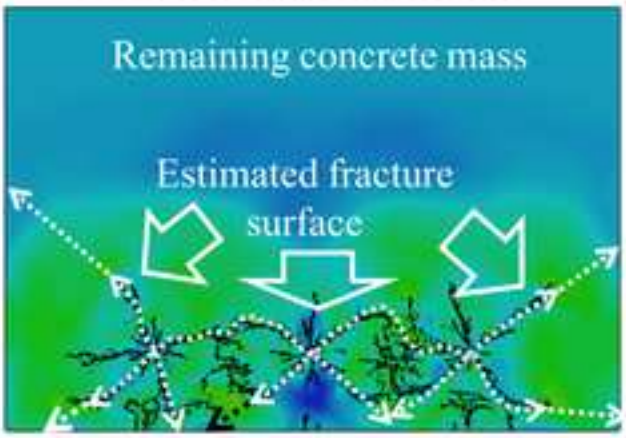

DFPA: Strength Distribution 3

The results of DFPAs are t = 280 μs.

V_{NM} =12 mL.